Generation of broadband laser by high-frequency bulk phase modulator with multipass configuration

Peng Zhang,* Youen Jiang, Shenlei Zhou, Wei Fan, and Xuechun Li

National Laboratory of High Power Laser Physics, Shanghai Institute of Optics and Fine Mechanics, Chinese Academy of Sciences, Shanghai 201800, China

*Corresponding author: zplianhe@siom.ac.cn

Received 9 October 2014; accepted 30 October 2014;
posted 6 November 2014 (Doc. ID 224680); published 3 December 2014

A new technique is presented for obtaining a large broadband nanosecond-laser pulse. This technique is based on multipass phase modulation of a single-frequency nanosecond-laser pulse from the integrated front-end source, and it is able to shape the temporal profile of the pulse arbitrarily, making this approach attractive for high-energy-density physical experiments in current laser fusion facilities. Two kinds of cavity configuration for multipass modulation are proposed, and the performances of both of them are discussed theoretically in detail for the first time to our knowledge. Simulation results show that the bandwidth of the generated laser pulse by this approach can achieve more than 100 nm in principle if adjustment accuracy of the time interval between contiguous passes is controlled within 0.1% of a microwave period. In our preliminary experiment, a 2 ns laser pulse with 1.35-nm bandwidth in 1053 nm is produced via this technique, which agrees well with the theoretical result. Owing to an all-solid-state structure, the energy of the pulse achieves 25 μJ. In the future, with energy compensation and spectrum filtering, this technique is expected to generate a nanosecond-laser pulse of 3 nm or above bandwidth with energy of about 100 μJ.

OCIS codes: (060.5060) Phase modulation; (140.3518) Lasers, frequency modulated; (140.3300) Laser beam shaping; (140.3580) Lasers, solid-state; (350.2660) Fusion.

http://dx.doi.org/10.1364/AO.53.008229

1. Introduction

High-power laser facilities like the National Ignition Facility in the United States and Laser MegaJoule in France are designed to create the ignition of a deuterium–tritium nuclear fusion target in a laboratory setting [1,2]. In such a large laser system, a broadband laser plays a crucial role in many aspects. First, it can be used in smoothing by spectral dispersion (SSD) to achieve the required irradiation uniformity on the target [3–11]. A large broadband laser is desired since the amount of bandwidth determines the rate of smoothing, which must be accomplished before the target can significantly respond to the laser nonuniformity [5,6,8]. Second, a large laser bandwidth can significantly reduce parametric instabilities in high-intensity laser–plasma interaction (LPI), such as stimulated Raman scattering and simulated Brillouin scattering [12–18]. These parametric instabilities can cause poor coupling of laser beams onto the target. Broadband laser is desirable in LPI because the power of the laser is dispersed over a frequency range $\Delta\omega$, which may exceed the bandwidth γ associated with parametric instabilities. The frequencies of light outside the instability bandwidth will not be able to drive parametric instabilities. Therefore, the effective power that is available to drive instabilities is reduced by the factor $\gamma/\Delta\omega$.

There are mainly two approaches to generate a nanosecond broadband laser pulse. The first one is stretching an ultrashort pulse produced by a mode-locked laser to a duration of nanoseconds by a grating

1559-128X/14/358229-11$15.00/0

stretcher [19]. This method is simple and direct, yet the nanosecond-laser pulse produced in this way is unable to flexibly change its temporal shape to meet the requirements of a wide range of high-energy-density physical experiments. Another approach is phase modulating an nanosecond optical pulse from an integrated front-end source (IFES) that generates a single-frequency pulse at 1053 nm [1]. Although a nanosecond-laser pulse with an arbitrarily shaped temporal profile can be obtained in this way, the disadvantage is that the bandwidth of the laser pulse is merely 0.3–0.5 nm [20], limited to the microwave power delivered to the phase modulator P_{rf}, which determines the modulation index of the modulator δ for a constant electro-optic (EO) crystal length L. If the problem of limitation of the modulation index can be solved, the bandwidth of the modulated beam is expected to be comparable to or even larger than that of a mode-locked oscillator.

Phase modulation in a multipass configuration is an effective solution to this problem and was first proposed in an all-fiber architecture by van Howe *et al.* [21]. The principle of this technique is using a phase modulator driven at low RF power in a fiber loop to simulate many stacked phase modulators. On this basis, Xin and Zuegel developed a directly chirped laser source which was expected to generate a 2.5-ns laser pulse with 0.78-nm bandwidth in 1053 nm by a similar experiment configuration [22]. However, there are two deficiencies for the application of this broadband fiber laser source in high power laser systems: first, the laser pulse traveled in the fiber ring a lot of times, and the length of fiber it passed through was too long. Therefore, group velocity dispersion of the fiber gave rise to frequency-modulation-to-amplitude-modulation (FM-to-AM) conversion of the output pulse [23–25], which would detrimentally influence the laser performance and reduce the safe margin against damage to the optics. Second, the energy of the broadband laser pulse obtained in this way was only a few nanojoules since the multipass modulation loop was in an all-fiber architecture. The broadband laser pulse still needs to experience a gain of $\sim 10^{13}$ that raises its energy from ~1 nJ to ~20 kJ before injecting into a target chamber and frequency converting. The total gain is large enough to cause gain narrowing of the laser pulse during the amplification process, which will also lead to severe FM-to-AM conversion [26].

In this work, we propose a solid-state broadband laser source based on multipass phase modulation. Modulation performances of two kinds of cavity configuration are analyzed theoretically in detail for the first time. The tolerance of broadening the laser bandwidth by this technique is also discussed, and the result shows that if adjustment accuracy of the time interval between contiguous passes can be controlled within 0.1% of a microwave period, the bandwidth of the generated laser can reach more than 100 nm in principle. A preliminary experiment is carried out to validate the feasibility of this broadband laser source, and a nanosecond-laser pulse with 1.35-nm bandwidth in 1053 nm is acquired by this technique, which can be scalable up to 3 nm or above bandwidth. It should be noted that benefiting from the all-solid-state configuration, this broadband laser source has an energy capability of ~25 μJ, which will dramatically reduce the amount of FM-to-AM conversion due to gain narrowing during the preamplifier and main amplifier chains.

2. High-Frequency Standing Wave Bulk Phase Modulator

The high-frequency bulk phase modulator is a key component of our broadband nanosecond-laser source. A number of high-frequency bulk phase modulators were developed for the application of two-dimensional (2D) SSD [27–35]. Among all these designs, a velocity-matched lithium niobate ($LiNbO_3$) modulator employing a microwave resonant design is most promising because of its effective microwave power coupling and high Q factor [33–35]. A schematic of such a waveguide-coupled resonant bulk phase modulator is shown in Fig. 1. Microwave radiation is coupled into the $LiNbO_3$ crystal positioned in an air waveguide by a waveguide–coaxial adaptor and a TE_{10} waveguide. Because the dielectric constant of $LiNbO_3$ is much higher than that of air, the operating frequency is below the cutoff frequency of the air waveguide. Therefore, a high-Q standing-wave microwave resonator is formed in the $LiNbO_3$ crystal, performing at $TE_{10\,n}$ mode.

When a laser pulse with angular frequency ω_0 passes through this bulk phase modulator, the electric field of the output laser beam can be expressed by [3]

$$E(t) = E_0 e^{i(\omega_0 t + \delta \sin \omega_m t)} = E_0 \sum_{l=-\infty}^{\infty} J_l(\delta) e^{i(\omega + l\omega_m t)}, \quad (1)$$

where ω_m is the frequency of microwave imposed on the phase modulator, δ is the modulation index, $J_l(\delta)$

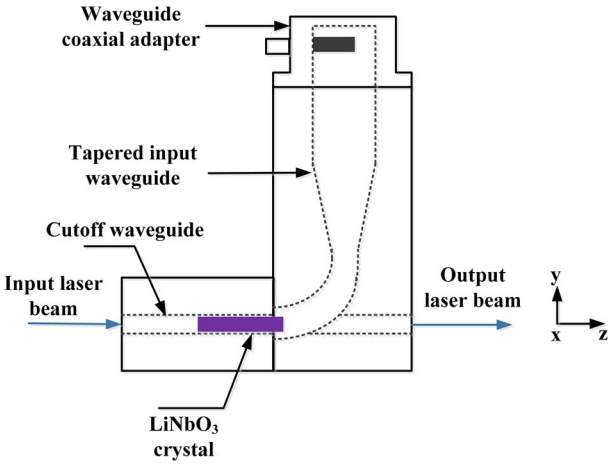

Fig. 1. Schematic of a microwave resonant bulk phase modulator.

is the Bessel function, and l is any integer. It can be seen from this expression that the laser spectrum is broadened by sinusoidal phase modulation. The spectral bandwidth produced by phase modulation can be approximately given by

$$\Delta\nu = \delta\omega_m/\pi. \tag{2}$$

Due to the cutoff-waveguide coupled resonator design, the microwave wave is imposed across the EO crystal in the form of standing waves, which can be decomposed into fields copropagating and counterpropagating with the laser beam. Since the sign of the space phase terms of copropagating and counterpropagating microwaves are opposite, the expressions of copropagating and counterpropagating microwave fields cannot be incorporated normally. Thus the analytical expression of δ cannot be obtained directly and must be solved by a numerical method.

Ignoring phase shifts associated with the reflections at the cutoff waveguide, the electrical fields of microwaves traveling along the $+z$ and $-z$ directions can be written as

$$E_{m\pm} = E_{m0}\cos\,\omega_m(t\mp z/v_{rf}), \tag{3}$$

where v_{rf} represents microwave velocity in the EO crystal.

When the laser pulse propagates along the z axis in Fig. 1, and both the optic and microwave vectors are along the y direction, the optical refraction index in $LiNbO_3$ crystal is given by

$$n = n_e - \frac{1}{2}r_{33}n_e^3(E_{m+} + E_{m-}), \tag{4}$$

where n_e is refraction index and r_{33} is the EO coefficient. The optical phase retardation at z in a single pass can be expressed by [36]

$$\Gamma_{\text{single}} = \frac{2\pi}{\lambda}\int_0^z n(z')\mathrm{d}z'. \tag{5}$$

Assuming the laser beam travels along the $+z$ axis and is at $z = 0$ at time $t = t_0$, it is at point z when

$$t = \frac{z}{v_{\text{opt}}} + t_0, \tag{6}$$

where v_{opt} is the optical group velocity in the EO crystal.

Inserting Eq. (6) into Eq. (3), and using Eqs. (4) and (5), the optical phase retardation at point z can be rewritten as

$$\Gamma_{\text{single}}(z) = \Gamma_0 - \frac{\pi n_e^3 r_{33}E_{m0}z}{\lambda}\left[\frac{\sin(u_+)}{u_+}\cos(\omega_m t_0 + u_+) + \frac{\sin(u_-)}{u_-}\cos(\omega_m t_0 + u_-)\right], \tag{7}$$

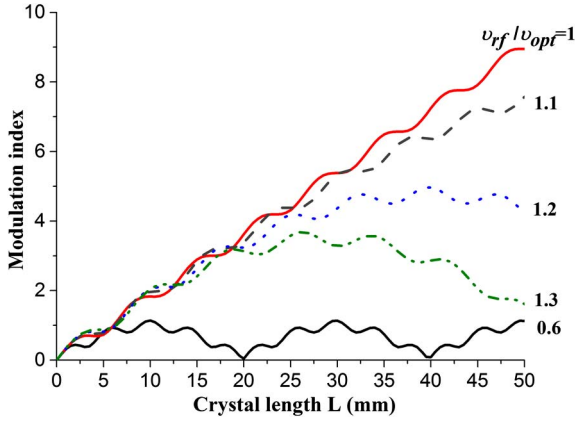

Fig. 2. Relationship between modulation index and crystal length in $LiNbO_3$ for several different velocity-matching conditions.

where Γ_0 is a time-independent phase retardation, and $u_\pm$ are the copropagating and counterpropagating velocity-mismatch reduction factors, which are given by

$$u_\pm = \frac{\omega_m z}{2}\left(\frac{1}{v_{\text{opt}}} \mp \frac{1}{v_{rf}}\right). \tag{8}$$

Ignoring Γ_0, which does not contribute to phase modulation of the laser beam (if not mentioned particularly, time-independent phase retardations will be neglected in the remainder of this paper), Eq. (7) can be written as

$$\Gamma_{\text{single}}(z) = -\frac{\pi n_e^3 r_{33}E_{m0}z}{\lambda}\left[\frac{\sin(u_+)}{u_+}\cos(\omega_m t_0 + u_+) + \frac{\sin(u_-)}{u_-}\cos(\omega_m t_0 + u_-)\right]. \tag{9}$$

Now, $\Gamma_{\text{single}}(z)$ in Eq. (9) is equivalent to the modulated phase term $\delta\sin\omega_m t$ in Eq. (1). Using Eqs. (8) and (9), the relationship between modulation index δ and crystal length L under different velocity-matching conditions for a modulation of 10.5 GHz can be obtained, which is plotted in Fig. 2. Agreeing with [34], the effective interaction length increases with degrees of velocity matching of the laser beam and microwave. The red solid curve represents a rigid-velocity-matched design, and there is a flat region between $L = 22$ and $L = 26$ mm. If velocity mismatch is controlled within 10% ($1 \le v_{rf}/v_{\text{opt}} \le 1.1$), the modulation index for $L = 23$ mm is comparable to or even larger than that of a rigid-velocity-matched design. Thus, $v_{rf}/v_{\text{opt}} = 1.1$ and $L = 23$ mm are chosen for our design. It should be noted that the analytical expression of velocity-mismatch reduction β in [34] is not rigorous because the different space phase terms of standing microwaves are not considered, which are very important for the analysis of phase matching for multipass phase modulation, which will be investigated below. Also

for this reason, the effective interaction lengths plotted in Fig. 2 are slightly larger than those obtained in [34] under the same velocity-matching conditions.

3. Multipass Phase Modulation Configuration Design

It can be inferred from Eq. (9) that the modulation index of a standing-wave EO phase modulator can be expressed by

$$\delta = \beta L \cdot (\pi n_e^3 r_{33} E_{m0})/\lambda, \tag{10}$$

where β is a velocity-mismatch reduction factor which takes into account influences of both copropagating and counterpropagating microwave velocity mismatch with the laser beam in a EO crystal. In general, β can only be calculated by a numerical method because of the different space phase terms between standing microwaves mentioned above.

From Eqs. (2) and (10), it can be seen that the bandwidth of the phase modulated laser beam is proportional to both of the EO crystal length and microwave power. Concerning the cost and volume of the microwave source, microwave power imposed on the EO crystal is finite in practice. And the EO crystal length is limited to about 23 mm to ensure effective modulation efficiency under certain velocity-matching conditions. Therefore, the bandwidth of the laser beam after a single-pass phase modulation is limited to merely 0.35 nm.

If the laser beam passes through a phase modulator more than once, and in each pass a rigid phase matching condition is satisfied, phase modulation can be accumulated effectively as the number of passes increases. To realize multipass modulation, an optical cavity should be designed to make a laser pulse pass through the modulator many times. There are mainly two types of cavity configuration suitable for multipass modulation: a linear cavity and a ring cavity, which will be discussed separately below.

A. Multipass Phase Modulation in a Ring Cavity Configuration

Figure 3 presents a sketch of a ring optical cavity configuration for multipass phase modulation. In each pass, a laser pulse enters the modulator from surface A and exits the modulator from surface B. Highly reflective mirrors M5 and M6, which simultaneously move along the z axis, act as a horizontal retroreflector, which is used for adjusting the time interval between contiguous passes

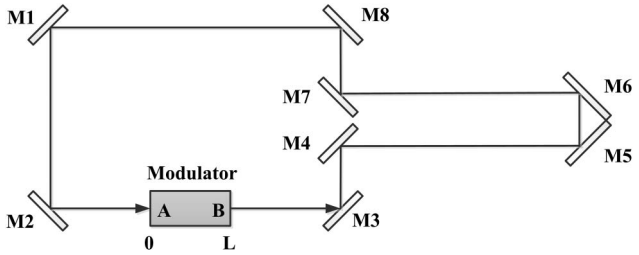

Fig. 3. Schematic of a ring cavity configuration for multipass phase modulation.

$$\Delta T_{\text{ring}} = \frac{L}{v_{\text{opt}}} + \frac{d}{c}, \tag{11}$$

where d is the distance from surface B in the previous pass to surface A in the latter pass.

For multipass modulation in the ring cavity configuration, assuming the laser beam is at $z = 0$ in the first pass at time $t = t_0$, it is at point z in the kth pass when

$$\begin{aligned} t &= (k-1)\left(\frac{L}{v_{\text{opt}}} + \frac{d}{c}\right) + \frac{z}{v_{\text{opt}}} + t_0 \\ &= (k-1)\Delta T_{\text{ring}} + \frac{z}{v_{\text{opt}}} + t_0, \end{aligned} \tag{12}$$

where k is zero or any positive integer. Using Eqs. (3), (4), and (5), phase retardation in the kth pass can be obtained:

$$\begin{aligned} \Gamma_k(z) = -\frac{\pi n_e^3 r_{33} E_{m0} z}{\lambda} \Bigg\{ &\frac{\sin(u_+)}{u_+} \cos\{\omega_m[(k-1)\Delta T_{\text{ring}} \\ &+ t_0] + u_+\} + \frac{\sin(u_-)}{u_-} \cos\{\omega_m[(k-1)\Delta T_{\text{ring}} \\ &+ t_0] + u_-\} \Bigg\}, \end{aligned} \tag{13}$$

and the total phase retardation of multipass modulation is

$$\begin{aligned} \Gamma_{\text{total}} &= \sum_{k=1}^{N} \Gamma_k(L) \\ &= -\frac{\pi n_e^3 r_{33} E_{m0} L}{\lambda} \sum_{k=1}^{N} \Bigg\{ \frac{\sin(u_+)}{u_+} \cos\{\omega_m[(k-1)\Delta T_{\text{ring}} \\ &+ t_0] + u_+\} + \frac{\sin(u_-)}{u_-} \cos\{\omega_m[(k-1)\Delta T_{\text{ring}} + t_0] \\ &+ u_-\} \Bigg\}, \end{aligned} \tag{14}$$

where N is the number of passes.

Equation (14) shows that when ΔT_{ring} equals an integral multiple of microwave period $T_m = 1/f_m$, the phase retardation in each pass is the same, equal to that in the first pass Γ_1. Therefore, Eq. (14) can be simplified as $\Gamma_{\text{total}} = N\Gamma_1$. In this case, the phase-matching condition is satisfied, and the modulation index increases as the number of passes grows, as shown in Fig. 4(a). In practice, due to adjustment accuracy of d, the time interval between contiguous passes is more or less deviated from an integral multiple of T_m. In that case, the phase-matching condition between contiguous passes is not rigidly satisfied, and the modulation index will grow within a finite number of passes. The amount of phase mismatch will accumulate as the number of passes increases. And finally, when the amount of phase

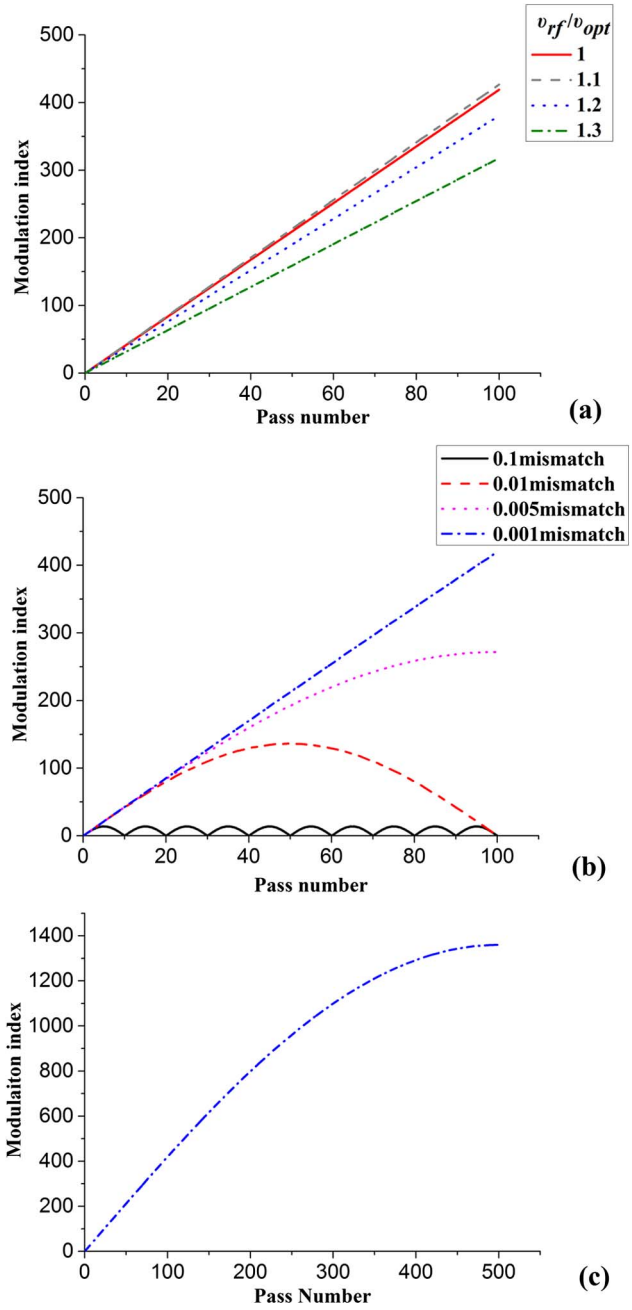

Fig. 4. Performance of multipass phase modulation in a ring cavity configuration. (a) Relationship between modulation index and pass number for different velocity-matching conditions when phase matching between each pass is rigidly satisfied. (b) Tolerance of accumulation of multipass modulation index for different adjustment accuracy conditions. $L = 23$ mm is selected as the EO crystal length, and the velocity mismatching factor is $v_{rf}/v_{\text{opt}} = 1.1$. (c) Tolerance of accumulation of multipass modulation index for adjustment accuracy of $0.001T_m$ displayed in scale of 100 pass number/div.

mismatching adds up to π, the modulation index achieves its maximum. Figure 4(b) shows the tolerance of accumulation of modulation index via multipass modulation for different adjustment accuracy conditions. It can be inferred from Fig. 4(b) that a larger modulation index can be obtained by multipass modulation for higher adjustment accuracy of d. When ΔT_{ring} is adjusted to the value which is $0.001T_m$ deviated from an integral multiple of T_m, the number of effective passes can be larger than 490, and the accumulated modulation index can reach 1360, corresponding to a bandwidth of 105.6 nm, which is shown in Fig. 4(c).

B. Multipass Phase Modulation in a Linear Cavity Configuration

The linear cavity configuration for multipass phase modulation is shown schematically in Fig. 5. Multipass modulation is realized by reflecting an optical pulse back and forth through the modulator. Two end mirrors M1 and M2 are used for adjusting phase matching in odd passes and even passes, respectively. Unlike a ring cavity configuration, in which the modulation index in each pass is the same when the phase-matching condition is satisfied, the performance of a linear multipass modulation cavity in even passes is generally different from that in odd passes, which makes multipass modulation in a linear cavity configuration exhibit distinctive characteristics.

In odd passes, a laser pulse passes through the modulator from surface A to surface B in Fig. 5. Similar to the ring cavity configuration, assuming the laser beam is at $z = 0$ in the first pass at time $t = t_0$, phase retardation at point z in the $(2k-1)$th pass is given by

$$\Gamma_{2k-1}(z) = -\frac{\pi n_e^3 r_{33} E_{m0} z}{\lambda}\left\{\frac{\sin(u_+)}{u_+}\cos\{\omega_m[2(k-1)\Delta T_{\text{linear}} + t_0] + u_+\} + \frac{\sin(u_-)}{u_-}\cos\{\omega_m[2(k-1)\Delta T_{\text{linear}} + t_0] + u_-\}\right\}, \tag{15}$$

where ΔT_{linear} is the time interval between contiguous passes in a linear cavity configuration, which is given by

$$\Delta T_{\text{linear}} = \frac{L}{v_{\text{opt}}} + \frac{2d}{c}.$$

In even passes, the laser pulse passes through the modulator from surface B to surface A, and it is at point z in the $2k$th pass when

$$t = (2k-1)\Delta T_{\text{linear}} + \frac{L-z}{v_{\text{opt}}} + t_0. \tag{16}$$

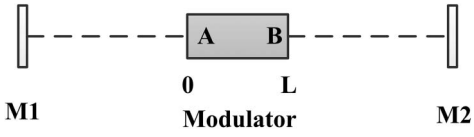

Fig. 5. Schematic of a linear cavity configuration for multipass phase modulation.

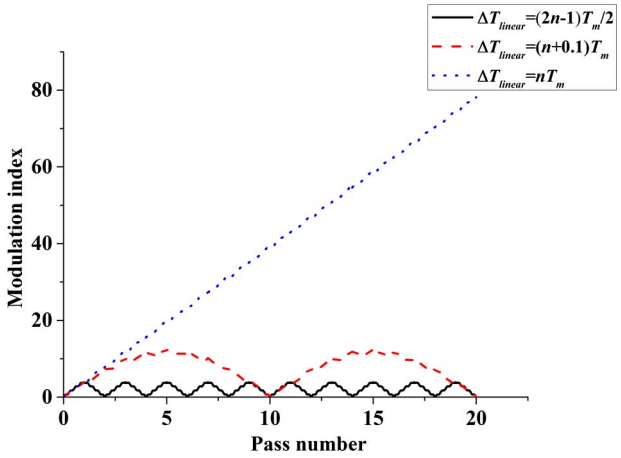

Fig. 6. Relationship between modulation index and the number of passes for different time interval values between contiguous passes when $L/v_{rf} = qT_m$.

Using Eq. (4), the refraction index at point z in the $2k$th pass is given by

$$\begin{aligned} n_{2k} &= -\frac{1}{2} r_{33} n_e^3 (E_{m+} + E_{m-}) \\ &= -\frac{1}{2} r_{33} n_e^3 \left\{ E_{0m} \cos \omega_m \left[t_0 + (2k-1)\Delta T_{\text{linear}} \right. \right. \\ &\quad \left. + \left(\frac{L-z}{v_{\text{opt}}} - \frac{z}{v_{rf}} \right) \right] + E_{0m} \cos \omega_m \left[t_0 + (2k-1)\Delta T_{\text{linear}} \right. \\ &\quad \left. \left. + \left(\frac{L-z}{v_{\text{opt}}} + \frac{z}{v_{rf}} \right) \right] \right\}. \end{aligned} \tag{17}$$

Let us introduce the distance between the position of the laser pulse in the EO crystal and the entrance face of even passes (surface B) z_1 as

$$z_1 = L - z. \tag{18}$$

Then phase retardation in the $2k$th pass can be obtained by using Eqs. (5), (17), and (18):

$$\begin{aligned} \Gamma_{2k}(z_1) = -\frac{\pi n_e^3 r_{33} E_{m0} z_1}{\lambda} &\left\{ \frac{\sin(u_+)}{u_+} \cos\left\{ \omega_m \left[(2k-1) \right. \right. \right. \\ &\left. \Delta T_{\text{linear}} + t_0 + \frac{L}{v_{rf}} \right] + u_+ \Big\} + \frac{\sin(u_-)}{u_-} \\ &\left. \cos\left\{ \omega_m \left[(2k-1)\Delta T_{\text{linear}} + t_0 - \frac{L}{v_{rf}} \right] + u_- \right\} \right\}. \end{aligned} \tag{19}$$

It can be seen that there is an additional phase term $\Delta\phi_\pm = \pm\omega_m L/v_{rf}$ for phase retardation in even passes compared with that in odd passes. This makes the features of multipass modulation in a linear cavity configuration different from that in a ring cavity configuration. The performance of multipass modulation for different values of L/v_{rf} in a linear cavity configuration will be discussed in detail below.

1. Performance of Multipass Modulation in a Linear Cavity Configuration when $L/v_{rf} = qT_m$ (q Is Any Positive Integer)

In this case, when the time interval between contiguous passes $\Delta T_{\text{linear}} = nT_m$, where n is any positive integer, using Eqs. (15) and (19), the phase retardations of odd and even passes are equal:

$$\begin{aligned} \Gamma_{2k-1}(L) &= \Gamma_{2k}(L) \\ &= -\frac{\pi n_e^3 r_{33} E_{m0} L}{\lambda} \left[\frac{\sin(u_+)}{u_+} \cos(\omega_m t_0 \right. \\ &\quad \left. + u_+) + \frac{\sin(u_-)}{u_-} \cos(\omega_m t_0 + u_-) \right]. \end{aligned} \tag{20}$$

By substituting Eq. (20) into Eq. (14), the total phase retardation of N-pass modulation is given by

$$\begin{aligned} \Gamma_{\text{total}} &= N\Gamma_1(L) \\ &= -\frac{\pi n_e^3 r_{33} E_{m0} NL}{\lambda} \left[\frac{\sin(u_+)}{u_+} \cos(\omega_m t_0 + u_+) \right. \\ &\quad \left. + \frac{\sin(u_-)}{u_-} \cos(\omega_m t_0 + u_-) \right], \end{aligned} \tag{21}$$

which grows linearly with an increasing number of passes.

When time interval $\Delta T_{\text{linear}} = (2n-1)T_m/2$, phase retardation of even passes equals the negative value of that of odd passes:

$$\begin{aligned} \Gamma_{2k}(L) &= -\Gamma_{2k-1}(L) \\ &= \frac{\pi n_e^3 r_{33} E_{m0} L}{\lambda} \left[\frac{\sin(u_+)}{u_+} \cos(\omega_m t_0 \right. \\ &\quad \left. + u_+) + \frac{\sin(u_-)}{u_-} \cos(\omega_m t_0 + u_-) \right], \end{aligned} \tag{22}$$

which indicates phase modulation in even passes and that in odd passes are completely mismatching. The total phase retardation is

$$\Gamma_{\text{total}} = \begin{cases} \Gamma_1(L) & N \text{ is odd number} \\ 0 & N \text{ is even number} \end{cases}. \tag{23}$$

When ΔT_{linear} equals a value between $(2n-1)T_m/2$ and nT_m, the phase retardations of odd passes and even passes are partly mismatched. And within a finite number of passes, the modulation index grows as the number of passes increases. Figure 6 plots modulation index as a function of number of passes for different time interval values when $L/v_{rf} = qT_m$.

2. Performance of Multipass Modulation in a Linear Cavity Configuration when $L/v_{rf} = (2q-1)T_m/2$ (q Is Any Positive Integer)

In this case, when time interval $\Delta T_{\text{linear}} = (2n-1)T_m/2$, where n is any positive integer, using Eqs. (15) and (19), the phase retardation of even passes equals that of odd passes. The phase modulation in even passes and that in odd passes are rigidly matching, and the total phase retardation is given by

$$\Gamma_{\text{total}} = N\Gamma_1(L) = -\frac{\pi n_e^3 r_{33} E_{m0} NL}{\lambda}\left[\frac{\sin(u_+)}{u_+}\cos(\omega_m t_0 + u_+) + \frac{\sin(u_-)}{u_-}\cos(\omega_m t_0 + u_-)\right]. \quad (24)$$

When the time interval between contiguous passes $\Delta T_{\text{linear}} = nT_m$, the phase retardation of even passes equals the negative value of that of odd passes. The phase modulation in even passes and that in odd passes are completely mismatching, and the total phase retardation is given by

$$\Gamma_{\text{total}} = \begin{cases} \Gamma_1(L) & N \text{ is odd number} \\ 0 & N \text{ is even number} \end{cases}. \quad (25)$$

When ΔT_{linear} equals a value between $(2n-1)T_m/2$ and nT_m, the phase retardation of odd passes and even passes are partly mismatched. And within a finite number of passes, the modulation index grows as the number of passes increases. Figure 7 plots modulation index as a function of number of passes for different time interval values when $L/v_{rf} = (2q-1)T_m/2$.

3. Performance of Multipass Modulation in a Linear Cavity Configuration when $(2q-1)T_m/2 < L/v_{rf} < qT_m$ (q Is Any Positive Integer)

Phase velocity mismatching factor v_{rf}/v_{opt} is set at different values near 1 to realize different L/v_{rf} conditions, which are shown in Table 1. The EO crystal length is selected as 23 mm here.

Table 1. Different L/v_{rf} Conditions by Setting *Rf* Velocity Value

v_{rf}/v_{opt}	L/v_{rf}
1.1571	$1.5T_m$
1.0848	$1.6T_m$
1.0210	$1.7T_m$
0.9918	$1.75T_m$
0.9643	$1.8T_m$
0.9135	$1.9T_m$
0.8678	$2T_m$

Using Eqs. (14), (15), and (19), multipass modulation performance in a linear cavity configuration for different L/v_{rf} conditions when time interval $\Delta T_{\text{linear}} = (2n-1)T_m/2$ and nT_m are shown respectively in Figs. 8(a) and 8(b). It can be seen that when the value of L/v_{rf} is closer to $(2q-1)T_m/2$ than to qT_m, the time interval between contiguous passes ΔT_{linear} should be set as $(2n-1)T_m/2$ to acquire the maximum multipass modulation index, where n is any positive integer number. Otherwise, when the value of L/v_{rf} is closer to qT_m, ΔT_{linear} should be set as nT_m to acquire the maximum multipass modulation index.

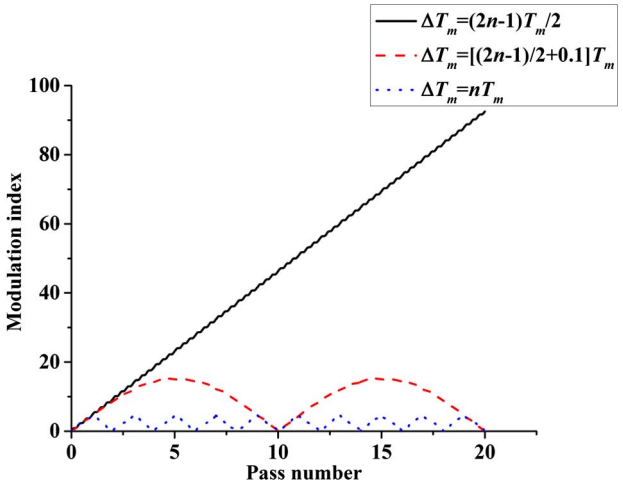

Fig. 7. Relationship between modulation index and the number of passes for various different time interval values between contiguous passes when $L/v_{rf} = (2q-1)T_m/2$.

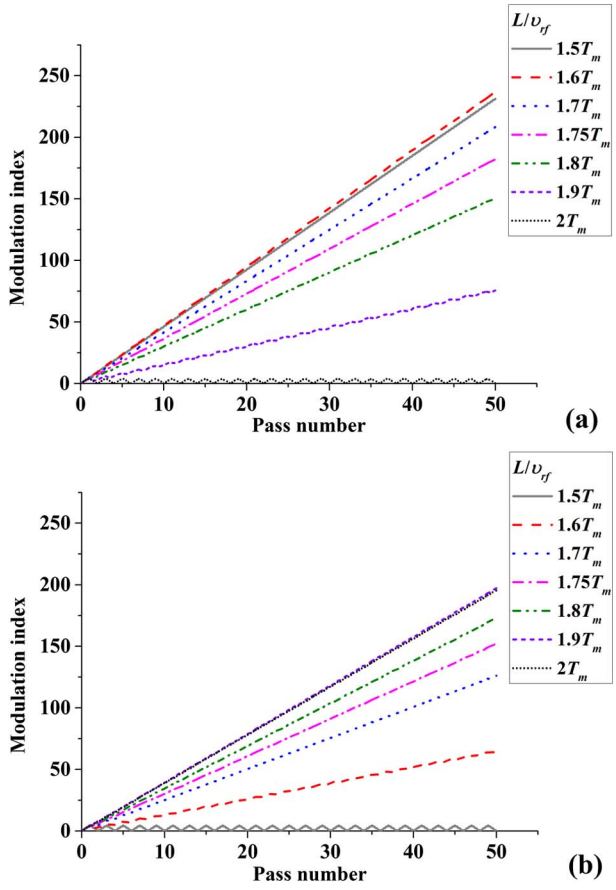

Fig. 8. Relationship between modulation index and the number of passes for various different L/v_{rf} when time interval values equals $(2n-1)T_m/2$ (a) and nT_m (b).

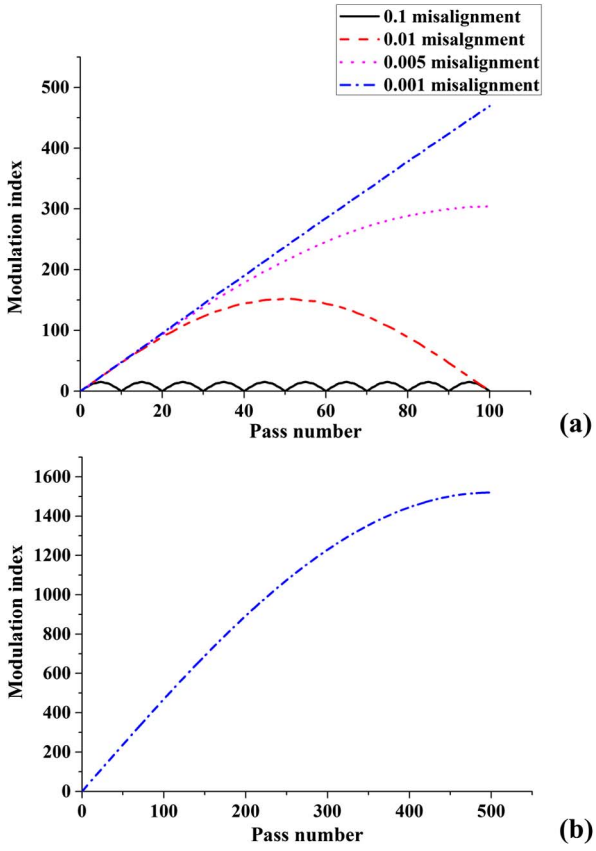

Fig. 9. (a) Tolerance of accumulation of multipass modulation index for different adjustment accuracy conditions in a linear cavity configuration. $L = 23$ mm is selected as the EO crystal length, and the velocity mismatching factor is set as $v_{rf}/v_{\text{opt}} = 1.1$. (b) Tolerance of accumulation of multipass modulation index for adjustment accuracy of 0.001 mismatching displayed in scale of 100 pass number/div.

Similar to the ring cavity configuration, tolerance of accumulation of multipass modulation for different adjustment accuracy of d in a linear cavity configuration can be obtained by Eqs. (14), (15), and (19), which is shown in Fig. 9. The EO crystal length is selected as 23 mm, and the velocity mismatching factor is set as 1.1 here. We can see that if ΔT_{linear} could be controlled within $0.001T_m$, the maximum modulation index will reach 1520, corresponding to 118.0 nm.

4. Experimental Setup

A preliminary experiment was carried out to verify the feasibility of this broadband laser source based on multipass phase modulation. A linear cavity configuration was employed since the cavity length of it is half of that of a ring cavity length. As shown in Fig. 10, the solid-state broadband nanosecond-laser source based on multipass phase modulation consists of a seed laser, a beam separation unit, and a multipass phase modulation resonator.

The seed laser comprises an IFES and an Nd-glass regenerative amplifier. The IFES creates a single-frequency nanosecond-laser pulse at 1053 nm and

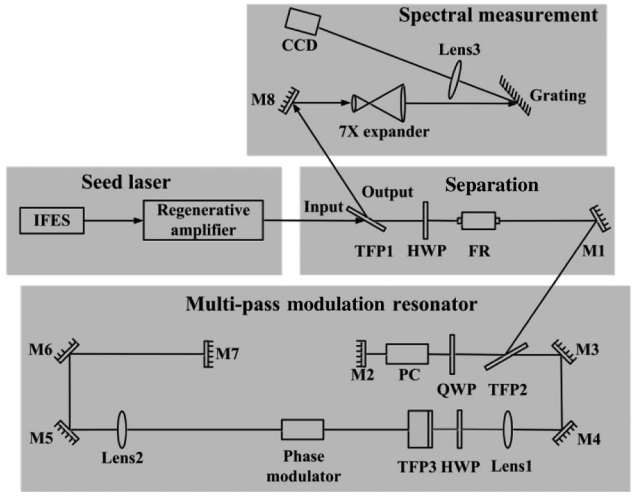

Fig. 10. Experimental setup of the solid-state broadband nanosecond-laser system and a grating spectrometer which is used for measuring spectrum distribution of the modulated output pulse.

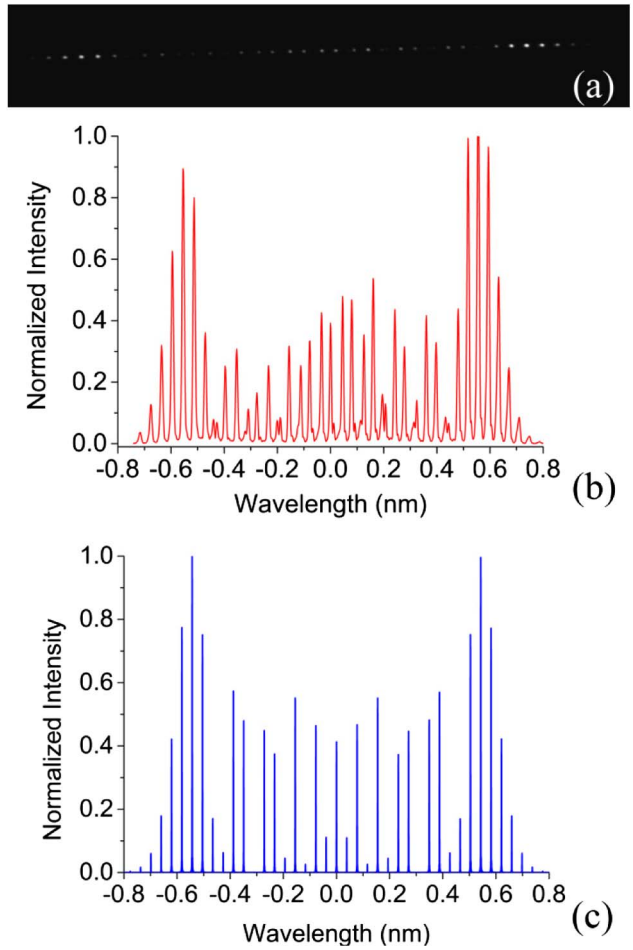

Fig. 11. Spectral measurement for the four-pass phase modulation with a grating spectrometer. (a) Grating spectrometer image of a four-pass phase-modulated 2 ns laser pulse. (b) Temporal spectrum converted from the grating spectrometer image. (c) Simulated spectrum for the four-pass phase modulation with the same modulation index.

is capable of flexibly changing the temporal shape of the laser pulse. After leaving the IFES, the pulse enters the regenerative amplifier, experiencing a gain that raises its energy from 1 nJ to 100 μJ. The regenerative amplifier output is *p*-polarized. A thin-film polarizer (TFP) in combination with a half-wave plate (HWP) and a Faraday rotator are used for separating the modulated broadband pulse from the input pulse, which also protects the seed laser against feedback from later optical components. This waveplate–rotator combination makes the polarization of the input seed pulse rotate 90 deg from *p* to *s*, and the output beam remains unchanged in *s*-polarization.

The seed pulse is injected into the multipass modulation resonator via TFP2 as shown in Fig. 10. After passing through a quarter-wave plate (QWP) twice, the beam polarization rotates 90 deg from *s* to *p*. Then the Pockels cell (PC) is switched on, trapping the pulse in the cavity for two round trips. During each round trip, the pulse passes through the bulk phase modulator twice. During the final pass, the PC is switched off, and the polarization of beam is transformed from *p* to *s* after passing through the QWP twice again. Then the laser pulse exits the cavity through TFP2. The combination of a HWP and TFP3 is used for adjusting the polarization of the beam in the EO crystal in the direction of the microwave vector. The bulk phase modulator, which can apply 0.35 nm bandwidth in a single-pass configuration with peak microwave pulse power of ~300 W, is located near the focal plane of a pair of confocal convex lenses to ensure that the beam passes through the EO crystal without blocking. The end mirrors

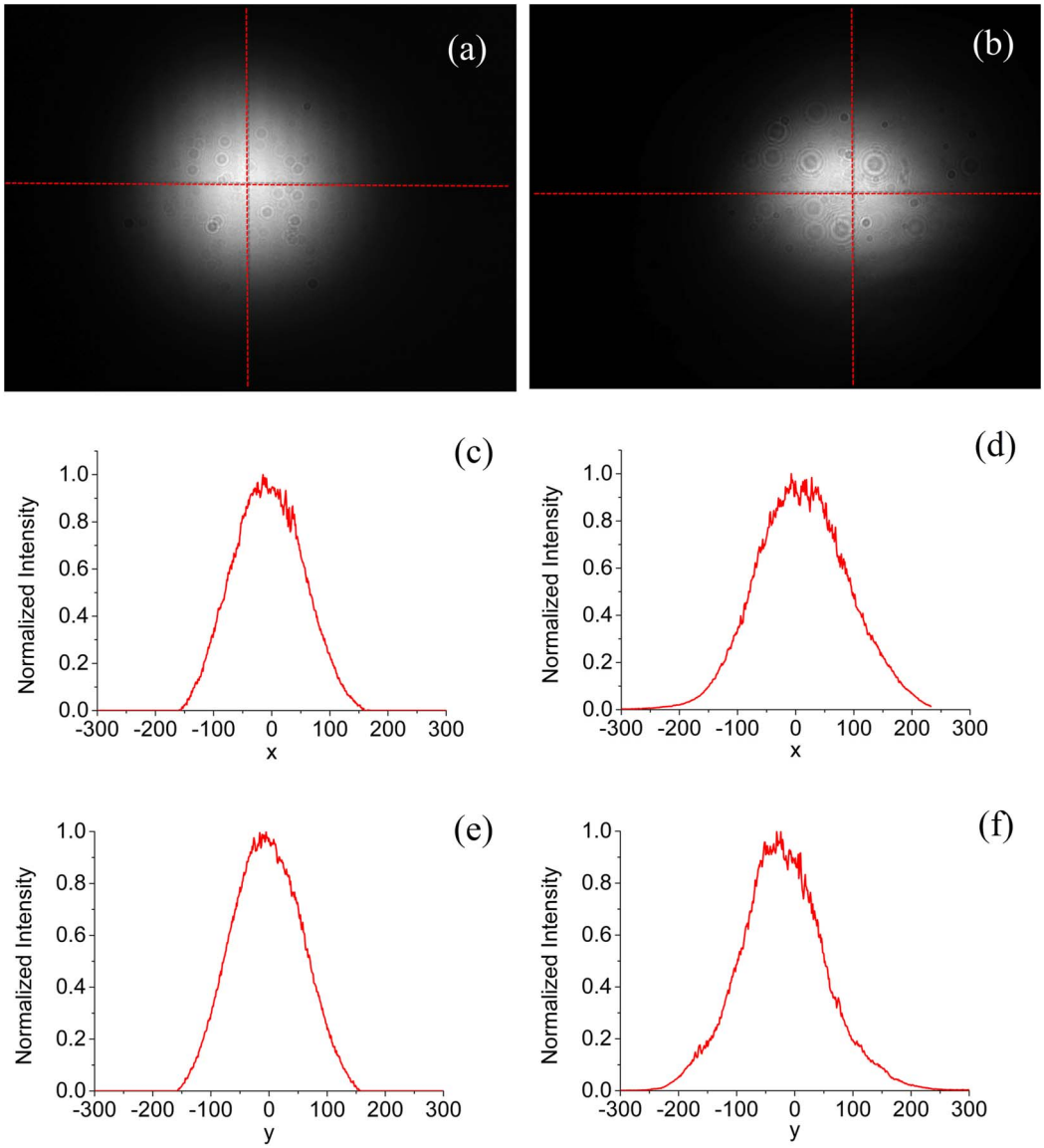

Fig. 12. Near field profiles of the (a) input beam and (b) four-pass modulated beam are measured by a CCD camera. (c) and (d) are single-line near field intensity distributions of the input beam and four-pass modulated beam, respectively, along the horizontal centerline direction. (e) and (f) are single-line near field intensity distributions of the input beam and four-pass modulated beam. respectively, along the vertical centerline direction.

M2 and M7 are positioned near the object and image plane of the confocal lenses, respectively, and are mounted on 1D linear stages which can be used for adjusting the distance between the end mirrors and the modulator to make the beam pulse and microwave satisfy the phase-matching condition in each pass.

5. Results and Discussion

The spectrum of the output of the broadband nanosecond-laser source is measured by a grating spectrometer, which consists of a 7× beam expander, a grating with a groove density of 1740 l/mm, a 1.5 m focal length lens, and a CCD.

Figure 11(a) shows the far-field intensity distribution of the broadband laser beam diffracted by the grating after four-pass phase modulation when the phase-matching condition in each pass is satisfied. The separated spots represent the resolving FM sidebands and the distance of two neighboring sidebands corresponds to 10.5 GHz bandwidth. Therefore, the spectrum of the four-pass phase modulated laser beam can be obtained, which is shown in Fig. 11(b). It can be seen that via four-pass phase modulation with microwave driven power of approximately 300 W, the spectral bandwidth of a 1053 nm, single-frequency, 2 ns pulse length laser is broadened to 1.35 nm. Since the single-pass modulation index of our bulk modulator is 4, the theoretical simulated spectrum of the four-pass modulated laser beam can be calculated by Eqs. (1), (2), and (24), which is shown in Fig. 11(c). It can be seen that the measured bandwidth agrees well with the theoretical results. The difference of the spectrum intensity distribution between experimental and theoretical results can be accounted for by the structure of the bulk phase modulator and the phase modulation deviating from a rigorous sinusoidal wave. It should be noted that the modulation performance of our modulator is worse than the performance of the one designed by Zuegel and Jacobs-Perkins at the University of Rochester, which can achieve FM bandwidths of up to 0.55 nm [34]. If we use the 10.4 GHz bulk modulator made by Rochester in our experiment, the total bandwidth of the output of our broadband laser source is expected to achieve ~2.2 nm after four-pass modulation.

Finally, we measured the near field profile of the input beam and four-pass modulated beam with a CCD camera. As shown in Fig. 12, a good quality near-Gaussian beam profile is obtained in both cases. It can be seen that the width of the vertical profile is a little shorter than that of the horizontal profile for the four-pass modulated beam. This is because the distance between the two lenses in the cavity has not been rigorously adjusted to two times the focal length. Therefore, as the number of passes increases, the dimension of the beam becomes larger. Since the vertical length of the $LiNbO_3$ crystal is shorter than the horizontal length, the vertical profile of the beam will be clipped by the EO crystal and the horizontal profile will pass through the crystal completely when the beam diameter is larger than vertical dimension and smaller than the horizontal dimension of the EO crystal. This problem can be solved completely if a shearing interferometer is used for precisely adjusting the distance between Lens1 and Lens2 to make the two lenses confocal. The spots appearing in the images are caused by dust particles on neutral gray filters and the CCD itself.

The output bandwidth of our broadband laser source, which is determined by the number of modulation passes, is limited by the energy loss in the cavity. The single-pass transmittance of the cavity is about 0.7, and the energy of the output laser pulse after four-pass modulation is 25 μJ. Bandwidth scaling beyond 3 nm with pulse energy of about the order of magnitude of 100 μJ may be possible if a Yb:glass amplifier head is used in the cavity for energy loss compensation. Meanwhile, a spectrum filtering technique should be employed in the setup to compensate the gain narrowing effect of Yb:glass.

6. Conclusions

A method of producing broadband nanosecond-laser pulses by a high-frequency bulk phase modulator with a multipass configuration has been proposed. The laser pulse generated in this way has the advantages of an arbitrarily shaped temporal profile, high output energy, and large spectrum bandwidth, which make this technique suitable for applications in inertial confinement fusion experiments, such as SSD technology and reducing parametric instabilities in high-intensity LPI.

Two cavity configurations, a ring and linear cavity configuration, were presented. The characteristics of their multipass modulation performance were analyzed theoretically for the first time. Compared to a ring cavity configuration, the modulation performance of a linear cavity configuration is more complex because of the influence of additional space terms of L/v_{rf} in even passes. The tolerances of accumulation of modulation index in both cavity configurations were analyzed, which were determined by the adjustment accuracy of the distances between end mirrors and the modulator. If the time interval between contiguous passes is controlled within $0.001T_m$, the number of effective modulation passes for both cavity configurations can achieve more than 490, corresponding to a laser bandwidth of 105.6 nm for a ring cavity configuration and 118.0 nm for a linear cavity configuration.

Finally, a preliminary experiment was carried out to validate the feasibility of this technique. A 2 ns laser pulse was generated with bandwidth up to 1.35 nm via four-pass phase modulation. The energy of this broadband pulse was 25 μJ without an active medium for energy compensation, and its near field intensity profile exhibits a good quality near-Gaussian distribution. It should be noted that the laser bandwidth is expected to achieve 3 nm or above with its output energy of the order of magnitude of

100 μJ if energy compensation and spectrum filtering are employed.

This research was supported by the National Natural Science Foundation of China (Project No. 61405211).

References

1. C. A. Haynam, P. J. Wegner, J. M. Auerbach, M. W. Bowers, S. N. Dixit, G. V. Erbert, G. M. Heestand, M. A. Henesian, M. R. Hermann, K. S. Jancaitis, K. R. Manes, C. D. Marshall, N. C. Mehta, J. Menapace, E. Moses, J. R. Murray, M. C. Nostrand, C. D. Orth, R. Patterson, R. A. Sacks, M. J. Shaw, M. Spaeth, S. B. Sutton, W. H. Williams, C. C. Widmayer, R. K. White, S. T. Yang, and B. M. Van Wonterghem, "National ignition facility laser performance status," Appl. Opt. **46**, 3276–3303 (2007).
2. C. Cavailler, "Inertial fusion with the LMJ," Plasma Phys. Controlled Fusion **47**, B389–B403 (2005).
3. S. Skupsky, R. W. Short, T. Kessler, R. S. Craxton, S. Letzring, and J. M. Soures, "Improved laser-beam uniformity using the angular-dispersion of frequency-modulated light," J. Appl. Phys. **66**, 3456–3462 (1989).
4. J. E. Rothenberg, "Two dimensional beam smoothing by spectral dispersion for direct drive inertial confinement fusion," Proc. SPIE **2633**, 634–644 (1995).
5. "Two-dimensional SSD on OMEGA," LLE Rev. **69**, 1–10 (1996).
6. J. E. Rothenberg, "Comparison of beam-smoothing methods for direct-drive inertial confinement fusion," J. Opt. Soc. Am. B **14**, 1664–1671 (1997).
7. J. A. Marozas and J. H. Kelly, "Angular spectrum representation of pulsed laser beams with two-dimensional smoothing by spectral dispersion," LLE Rev. **78**, 62–81 (1999).
8. S. Skupsky and R. S. Craxton, "Irradiation uniformity for high-compression laser-fusion experiments," Phys. Plasmas **6**, 2157–2163 (1999).
9. S. P. Regan, J. A. Marozas, J. H. Kelly, T. R. Boehly, W. R. Donaldson, P. A. Jaanimagi, R. L. Keck, T. J. Kessler, D. D. Meyerhofer, W. Seka, S. Skupsky, and V. A. Smalyuk, "Experimental investigation of smoothing by spectral dispersion," J. Opt. Soc. Am. B **17**, 1483–1489 (2000).
10. S. P. Regan, J. A. Marozas, R. S. Craxton, J. H. Kelly, W. R. Donaldson, P. A. Jaanimagi, D. Jacobs-Perkins, R. L. Keck, T. J. Kessler, D. D. Meyerhofer, T. C. Sangster, W. Seka, V. A. Smalyuk, S. Skupsky, and J. D. Zuegel, "Performance of 1-THz-bandwidth, two-dimensional smoothing by spectral dispersion and polarization smoothing of high-power, solid-state laser beams," J. Opt. Soc. Am. B **22**, 998–1002 (2005).
11. J. A. Marozas, T. J. B. Collins, and J. D. Zuegel, "Multiple-FM smoothing by spectral dispersion-an augmented laser speckle smoothing scheme," LLE Rev. **114**, 73–84 (2008).
12. D. Eimerl, E. M. Campbell, W. Krupke, J. Zweiback, W. L. Kruer, J. Marozas, J. Zuegel, J. Myatt, J. Kelly, D. Froula, and R. L. McCrory, "StarDriver: a flexible laser driver for inertial confinement fusion and high energy density physics," J. Fusion Energy **33**, 476–488 (2014).
13. J. J. Thomson, "Finite-bandwidth effects on parametric-instability in an inhomogeneous plasma," Nucl. Fusion **15**, 237–247 (1975).
14. K. Estabrook, J. Harte, E. M. Campbell, F. Ze, D. W. Phillion, M. D. Rosen, and J. T. Larsen, "Estimates of intensity, wavelength, and bandwidth scaling of Brillouin backscatter," Phys. Rev. Lett. **46**, 724–727 (1981).
15. K. Estabrook and W. L. Kruer, "Theory and simulation of one-dimensional Raman backward and forward scattering," Phys. Fluids **26**, 1892–1903 (1983).
16. W. H. Tan, Z. Q. Lin, M. Gu, A. Shi, W. Y. Yu, and X. M. Deng, "The influence of laser frequency bandwidth on the time and space resolved structures of the 2-omega-0 harmonic-generation," Phys. Fluids **30**, 1510–1514 (1987).
17. B. W. Boreham, H. Hora, M. Aydin, S. Eliezer, M. P. Goldsworthy, G. Min, A. K. Gahatak, P. Lalousis, R. J. Stening, H. Szichman, B. Luther-Davies, K. G. H. Baldwin, R. A. M. Maddever, and A. V. Rode, "Beam smoothing and temporal effects: optimized preparation of laser beams for direct-drive inertial confinement fusion," Laser Part. Beams **15**, 277–295 (1997).
18. G. Riazuelo and G. Bonnaud, "Coherence properties of a smoothed laser beam in a hot plasma," Phys. Plasmas **7**, 3841–3844 (2000).
19. M. D. Perry, D. Pennington, B. C. Stuart, G. Tietbohl, J. A. Britten, C. Brown, S. Herman, B. Golick, M. Kartz, J. Miller, H. T. Powell, M. Vergino, and V. Yanovsky, "Petawatt laser pulses," Opt. Lett. **24**, 160–162 (1999).
20. M. Bowers, S. Burkhart, S. Cohen, G. Erbert, J. Heebner, M. Hermann, and D. Jedlovec, "The injection laser system on the National Ignition Facility," Proc. SPIE **6451**, 64511M (2007).
21. J. van Howe, J. H. Lee, and C. Xu, "Generation of 3.5 nJ femtosecond pulses from a continuous-wave laser without mode locking," Opt. Lett. **32**, 1408–1410 (2007).
22. R. Xin and J. D. Zuegel, "Directly chirped laser source for chirped-pulse amplification," in *Lasers, Sources and Related Photonic Devices* (Optical Society of America, 2010), p. AMD3.
23. E. J. Bochove, E. M. Decarvalho, and J. E. R. Filho, "FM–AM conversion by material dispersion in an optical fiber," Opt. Lett. **6**, 58–60 (1981).
24. A. R. Chraplyvy, R. W. Tkach, L. L. Buhl, and R. C. Alferness, "Phase modulation to amplitude-modulation conversion of CW laser-light in optical fibers," Electron. Lett. **22**, 409–411 (1986).
25. X.-C. Tian, Z. Sui, Z.-H. Huang, H.-H. Lin, J.-J. Wang, R. Zhang, D.-P. Xu, Y.-L. Zhang, and N. Zhu, "Periodic linear chirped pulse generation based on direct phase modulation," Acta Phys. Sin. **62**, 104216 (2013).
26. S. Hocquet, D. Penninckx, E. Bordenave, C. Gouédard, and Y. Jaouën, "FM-to-AM conversion in high-power lasers," Appl. Opt. **47**, 3338–3349 (2008).
27. E. Bonek, M. Knecht, G. Magerl, K. Preis, and K. R. Richter, "Coupling and tuning of trapped-mode microwave resonators," AEU Int. J. Electron. C **32**, 209–214 (1978).
28. G. M. Carter, "Tunable high-efficiency microwave frequency-shifting of infrared-lasers," Appl. Phys. Lett. **32**, 810–812 (1978).
29. N. H. Tran, T. F. Gallagher, J. P. Watjen, G. R. Janik, and C. B. Carlisle, "High-efficiency resonant cavity microwave optical modulator," Appl. Opt. **24**, 4282–4284 (1985).
30. T. F. Gallagher, N. H. Tran, and J. P. Watjen, "Principles of a resonant cavity optical modulator," Appl. Opt. **25**, 510–514 (1986).
31. A. A. Godil, A. S. Hou, B. A. Auld, and D. M. Bloom, "Harmonic mode-locking of a Nd-Bel laser using a 20-GHz dielectric resonator optical modulator," Opt. Lett. **16**, 1765–1767 (1991).
32. F. Z. Guo, C. T. Yu, L. Chen, T. Kobayashi, and Y. Chen, "Quasi-velocity-matched electrooptic phase modulator for the synthesis of ultrashort optical pulses," IEEE J. Quantum Electron. **33**, 879–882 (1997).
33. J. D. Zuegel and J. A. Marozas, "High-frequency bulk phase modulator for broadband smoothing by spectral dispersion on OMEGA," LLE Rev. **78**, 53–61 (1999).
34. J. D. Zuegel and D. W. Jacobs-Perkins, "Efficient, high-frequency bulk phase modulator," Appl. Opt. **43**, 1946–1950 (2004).
35. Y. Jiang, X. Li, S. Zhou, W. Fan, and Z. Lin, "Microwave resonant electro-optic bulk phase modulator for two-dimensional smoothing byspectral dispersion in SG-II," Chin. Opt. Lett. **11**, 052301 (2013).
36. I. P. Kaminow and J. Liu, "Propagation characteristics of partially loaded two-conductor transmission line for broadband light modulators," Proc. IEEE **51**, 132–136 (1963).